Growth, coalescence, and etching of two-dimensional overlayers on metals modulated by near-surface Ar nanobubbles

Journal Article

Author(s):
Wei, Wei; Pan, Jiaqi; Lin, Haiping; Euaruksakul, Chanan; Li, Zhiyun; Huang, Rong; Wang, Li; Wang, Zhujun; Fu, Qiang; Cui, Yi

Research Article

Growth, coalescence, and etching of two-dimensional overlayers on metals modulated by near-surface Ar nanobubbles

Wei Wei[1], Jiaqi Pan[1], Haiping Lin[2], Chanan Euaruksakul[3], Zhiyun Li[1], Rong Huang[1], Li Wang[1], Zhujun Wang[4,5] (✉), Qiang Fu[6] (✉), and Yi Cui[1] (✉)

[1] *Vacuum Interconnected Nanotech Workstation, Suzhou Institute of Nano-Tech and Nano-Bionics, Chinese Academy of Sciences, Suzhou 215123, China*
[2] *Institute of Functional Nano & Soft Materials (FUNSOM), Soochow University, Suzhou 215123, China*
[3] *Synchrotron Light Research Institute, Nakhon Ratchasima 30000, Thailand*
[4] *School of Physical Science and Technology, Shanghai Tech University, Shanghai 200031, China*
[5] *Scientific Center for Optical and Electron Microscopy, ETH Zürich, 8093 Zürich, Switzerland*
[6] *State Key Laboratory of Catalysis, iChEM, Dalian Institute of Chemical Physics, the Chinese Academy of Sciences, Dalian 116023, China*

ABSTRACT

The synthesis of high-quality ultrathin overlayers is critically dependent on the surface structure of substrates, especially involving the overlayer–substrate interaction. By using *in situ* surface measurements, we demonstrate that the overlayer–substrate interaction can be tuned by doping near-surface Ar nanobubbles. The interfacial coupling strength significantly decreases with near-surface Ar nanobubbles, accompanying by an "anisotropic to isotropic" growth transformation. On the substrate containing near-surface Ar, the growth front crosses entire surface atomic steps in both uphill and downhill directions with no difference, and thus, the morphology of the two-dimensional (2D) overlayer exhibits a round-shape. Especially, the round-shaped 2D overlayers coalesce seamlessly with a growth acceleration in the approaching direction, which is barely observed in the synthesis of 2D materials. This can be attributed to the immigration lifetime and diffusion rate of growth species, which depends on the overlayer–substrate interaction and the surface catalysis. Furthermore, the "round to hexagon" morphological transition is achieved by etching-regrowth, revealing the inherent growth kinetics under quasi-freestanding conditions. These findings provide a novel promising way to modulate the growth, coalescence, and etching dynamics of 2D materials on solid surfaces by adjusting the strength of overlayer–substrate interaction, which contributes to optimization of large-scale production of 2D material crystals.

KEYWORDS

two dimensional materials, overlayer –substrate interaction, near-surface Ar nanobubbles, evolution behavior, surface dynamics

1   Introduction

The catalytic growth of two-dimensional (2D) materials on metal substrates by chemical vapor deposition (CVD) is the most widely used method to fabricate continuous films and meets the industrial demand for electronic-grade materials [1–6]. During CVD processes, the substrates serve as both catalysts for the decomposition of precursors and templates for 2D film growth; as a result, their surfaces are crucial in the overlayer nucleation, growth, and coalescence. Thus, the quality of overlayers is critically dependent on the overlayer–substrate interaction which can be orthogonally decomposed into the out-of-plane interaction (covalent interaction between film and metal) and in-plane interaction (interaction between the overlayer edge and the surface step of the substrate) [7–9].

Studies have demonstrated that the out-of-plane interaction can produce a moiré corrugation of overlayers, intensify in-plane interaction, and eventually modify the overlayer in-plane evolution mode. In strong overlayer–substrate interaction regimes, e.g., Ru and Re, the uphill growth is nearly inhibited. In the downhill direction, the overlayer extension induces the substrate surface rearrangement, as a result of a single-terrace growth [10–12]. These two factors result in the in-plane anisotropic growth. In weak overlayer–substrate interaction issues, such as Ir, Pt, and Cu, the growth front of the 2D film extends across both the uphill and downhill steps but the out-of-plane coupling strength can still induce in-plane anisotropic growth [13–16]. In quasi-freestanding regimes, such as 2D films on liquid metal or liquid glass, overlayers grow isotropically, indicating that in-plane interaction is fully removed [17–20]. Despite recent achievements, the influence of 2D overlayer–substrate interactions on the growth and coalescence behavior has not been systematically studied; consequently, the understanding of interfacial interactions during 2D film CVD processes is insufficient.

To better understand the effect of interfacial interactions on 2D evolution behavior, we need to develop a method for *in situ*

observation of 2D film growth by exclusively tuning the strength of the out-of-plane interaction and maintaining other parameters during the CVD process. Recent studies have demonstrated an effective method to tune the out-of-plane interaction by introducing near-surface species. Hoffman et al. have confirmed that near-surface C species weaken the interaction between graphene overlayers and Ni surfaces, leading to the formation of non-epitaxial graphene [21]. Similarly, our previous reports have indicated that the epitaxial feature of h-BN growth on Ni and Ru substrates depends on the near-surface B species which weakens the out-of-plane coupling strength [22]. However, in these studies, the near-surface species are from the precursor of 2D materials, and thus, the segregation of near-surface species still contributes to the growth. Consequently, possibilities of "only tuning out-of-plane coupling strength" are not addressed.

In this study, the neutral near-surface Ar nanobubbles with absence of CVD process, is introduced to systematically investigate the influence of overlayer–substrate interaction on the growth, coalescence, and etching of graphene on Ru(0001) surfaces by tuning out-of-plane coupling strength between overlayers and substrates. Graphene is a prototype 2D material, and key findings in our issue can be generalized to other 2D materials. It has been demonstrated that near-surface Ar nanobubbles significantly weaken the out-of-plane interaction, leading to the in-plane surface step restriction being nearly depleted, such that the overlayer growth mode transfers from anisotropy to isotropy. As a result, controlled growth of round-shaped graphene domains has been achieved by only tuning the out-of-plane coupling strength, thereby illustrating that the coupling strength between the overlayer and the substrate is a key factor in the shape evolution of 2D crystalline materials. Especially, the neighboring domains coalesce seamlessly, accompanying by an accelerated growth at the approaching frontiers. This abnormal coalescence behavior can be ascribed to the long immigration lifetime of growth species, because of the high hydrocarbon-dissociation activity from the surfaces and the very weak overlayer–substrate interaction. Besides, the "round to hexagon" morphological transition is realized by etching-regrowth, revealing the inherent growth-etching kinetics under quasi-freestanding conditions. These findings provide a novel and promising method to modulate the dynamic processes of 2D materials on surfaces.

2 Experimental section

2.1 Instruments

The main experiments were performed in the Vacuum Interconnected Nanotech Workstation (NANO-X) of Suzhou Institute of Nano-Tech and Nano-Bionics, Chinese Academy of Sciences. In this system, more than 20 instruments such as photoemission electron microscopy (PEEM)/low-energy electron microscopy (LEEM), scanning tunneling microscopy (STM), X-ray photoelectron spectroscopy (XPS) and time-of-flight secondary ion mass spectrometry (TOF-SIMS), are interconnected by ultrahigh vacuum (UHV) tubes where samples can be transferred from one endstation to another one. (1) Dynamic imaging experiments were performed in a SPECS PEEM/LEEM system which consisted of a preparation chamber and a main chamber (base pressure < 3 × 10^{-10} mbar). In LEEM mode the micro-region low energy electron diffraction (μ-LEED) can be performed to investigate the surface structure from local regions. (2) Local X-ray absorption spectroscopy (XAS) characterization based on X-ray PEEM (XPEEM) measurements was conducted at the XPEEM endstation of Synchrotron Light Research Institute (SLRI) in Thailand, which is installed with a preparation chamber

and a main chamber (base pressure < 2 × 10^{-10} mbar). Energy-filtered XPEEM images stack was collected to construct local XAS of small regions of interest (ROIs) by measuring the integrated intensity of the ROIs through the stack as a function of energy. The energy resolution of such local XAS is limited by the analyzer exit slit to be about 0.15 eV, while the lateral resolution of XPEEM image is below 30 nm. (3) Atomic resolution surface imaging was carried out in a SPECS STM instruments (base pressure < 2 × 10^{-10} mbar). (4) Depth resolution mass spectra were conducted on a TOF-SIMS 5-100 instrument (ION-TOF GmbH), which is connected with a UHV preparation chamber. The sputter ion source used Cs^+ ion with energy at 1 keV, beam current of 20.1 nA and raster size of 300 μm for the depth profile. And the analyses were carried out with a Bi^+ primary gun with a beam energy of 30 kV, beam current of 0.7 pA and raster size of 100 μm. (5) XPS analysis was performed on a XPS instrument (from PHI Corporation) based on micro-focused monochromatic Al Kα X-ray source scanning X-ray beam, which has a high energy resolution of 0.15 eV.

2.2 Sample preparation

(1) A Ru(0001) single crystal was cleaned by sputtering of Ar^+ ions (2.0 kV, 7 × 10^{-6} Torr Ar gas), oxidation in 5 × 10^{-7} Torr O_2 at 600 °C, and annealing to 1,400 °C in UHV, which was named as Ru(0001)$_{-CLE}$. (2) Ru(0001) surfaces containing near-surface Ar nanobubbles (denoted as Ru(0001)$_{-NSA}$) were obtained by Ar^+ sputtering (2.0 kV, 1 × 10^{-5} Torr Ar) for 50 min with the subsequent annealing at 800 °C for 5min, in which Ar atoms were introduced into the near-surface region and parts of them aggregated into Ar nanobubbles. (3) Graphene overlayers were prepared using C_2H_4 gases as the precursor with pressure of 1 × 10^{-8} Torr and the substrate temperatures between 770 and 900 °C. (4) The graphene etching experiments on the Ru(0001)$_{-NSA}$ surface were performed in 1 × 10^{-7} mbar O_2 gases at 700 °C.

2.3 Density functional theory (DFT) methods

The spin-polarized DFT calculations were carried out with the Vienna *ab initio* simulation package (VASP) code [23, 24]. The ion–electron interactions were described by the projector augmented wave (PAW) potentials. [25, 26]. The Perdew–Burke–Ernzerhof (PBE) function within a generalized gradient approximation (GGA) was employed to describe the exchange-correlation interactions [27]. The cutoff energy of plane wave basis was set as 450 eV. The Ru(0001) surface was mimicked with a (7 × 7) slab model (*a* = 18.94 Å), which consisted of 4 Ru atomic layers. To simply the calculation, the graphene adsorbed surface was constructed by the coupling of (8 × 8) graphene cell with this (7 × 7) Ru(0001) surface. A Monkhorst–Pack 2 × 2 × 1 k-point grid was adopted to sample the Brillouin zone. The van der Waals dispersion correction was applied using the DFT-D3 method [28]. A vacuum of 25 Å in the *z* direction was employed to avoid interactions between periodic images. The convergence criteria for the residual force and energy during structure relaxation were set to 0.01 eV/Å and 1 × 10^{-4} eV, respectively.

3 Results and discussion

The Ru(0001) surface was chosen as the substrate for graphene growth. First, the Ru(0001) surface strongly interacts with graphene overlayers, which provides more opportunities to weaken the coupling strength via modulation over a wide range [29]. Second, the surface adopts a high hydrocarbon-dissociation activity, promoting the growth efficiency of graphene overlayers [30, 31]. On this substrate, introduction of near-surface Ar nanobubbles, absence of any changes in surface composition, is

attainable to tune the coupling strength between the graphene overlayer and the Ru(0001) surface and keep the hydrocarbon-dissociation activity of the substrate unchanged.

3.1 Transition from anisotropic to isotropic growth of graphene on Ru(0001) by dosing near-surface Ar nanobubbles

All experiments were started by preparing Ru(0001)$_{-CLE}$ and Ru(0001)$_{-NSA}$, as described in detail in the methods section. Compared to the atomically flat Ru(0001)$_{-CLE}$ with straight steps (Figs. 1(a) and 1(b)), the Ru(0001)$_{-NSA}$ surfaces contain randomly distributed nanosized protrusions with height of 2 to 6 Å which are ascribed to the formation of near-surface Ar nanobubbles (Figs. 1(c) and 1(d)) [32]. Local XAS characterization from synchrotron-based XPEEM can provide direct evidence on the protrusions' composition, with a spatial resolution of 20 nm [33]. As can be seen in Fig. 1(e), resonances at 244.3, 247.5, and 249.6 eV are only observed on the Ru(0001)$_{-NSA}$ surfaces in good agreement with the XAS results for Ar clusters at metal surfaces, indicating that Ar nanobbules have been produced in the near-surface regions [34].

Graphene overlayers were grown on Ru(0001)$_{-CLE}$ and Ru(0001)$_{-NSA}$ surfaces by exposure to 1×10^{-8} mbar C_2H_4 (CVD process) at 800 °C, respectively. The as-prepared samples were transferred to TOF-SIMS through UHV tubes. Surface carbon signals were detected on both surfaces, and embedded Ar species were detected in the near-surface region with a depth of 1 nm (Fig. S1 in the Electronic Supplementary Material (ESM)). Owing to the 10 nm lateral resolution of TOF-SIMS, the element distribution profile implies that near-surface Ar species uniformly distribute at the near-surface region Ru(0001)$_{-NSA}$ surfaces and remain stable under the applied harsh growth conditions. As shown in Figs. 2(a) and 2(d), graphene domains with monolayer features have the same symmetry and periodicity on both surfaces. In particular, they exhibit a $(13 \times 13)_{-graphene}$ on $(12 \times 12)_{-Ru}$ moiré superstructure, which is considered as the typical graphene overlayers aligned on Ru(0001) surfaces [35]. More differences between the two surfaces can be found at the mesoscale. As illustrated in Fig. 2(b), graphene domains display a sector shape that is elongated along the terrace direction on Ru(0001)$_{-CLE}$ surfaces, following an in-plane anisotropic growth mode. This is because the graphene overlayers rapidly grow along steps and

across steps in the downhill direction (Figs. 2(b) and 2(c)). While nearly inhibited, growth across steps in the uphill direction is remarkably slower (Figs. 2(b) and 2(c)). This nearly suppressed uphill step crossing has been demonstrated by the strong interaction between surface steps and graphene domain boundaries, that is, the in-plane interaction [10, 36]. In contrast, round-shaped graphene domains form on Ru(0001)$_{-NSA}$ surfaces (Fig. 2(e)), implying an isotropic growth mode. There is almost no growth inhibition in the uphill direction and the graphene domains uniformly grow along steps, and across steps in both downhill and uphill directions. This type of growth indicates that the in-plane anisotropy from the strong in-plane interaction is significantly diminished, which can be attributed to the introduction of near-surface Ar nanobubbles.

As shown in Fig. 2(j), *in situ* XPS results which have been deconvoluted (the raw data is displayed in Fig. S2 in the ESM), show that the C 1s binding energy of graphene on Ru(0001)$_{-NSA}$ surfaces shifts down by 0.5 eV with respect to that of graphene on Ru(0001)$_{-CLE}$ surfaces. Besides, as shown by the inserts in Figs. 2(b) and 2(e), the intensity of the moiré pattern of graphnene/Ru(0001)$_{-NSA}$ becomes weaker than that of grapnene/Ru(0001)$_{-CLE}$. These two measurements confirm that
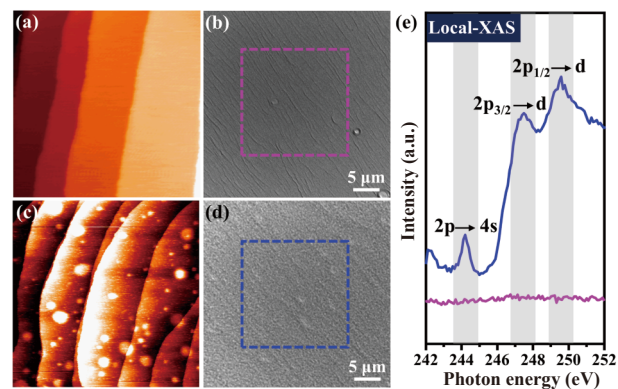
Figure 1 Formation of Ar nanobubbles in the near-surface regions of Ru(0001) surfaces. (a) STM image (200 nm × 200 nm) and (b) LEEM image of the Ru(0001)$_{-CLE}$ surface. (c) STM image (500 nm × 500 nm) and (d) LEEM image of the Ru(0001)$_{-NSA}$ surface. (e) Ar local XAS spectra based on XPEEM acquired from ROIs inside the purple and blue dotted boxes on the Ru(0001)$_{-CLE}$ and Ru(0001)$_{-NSA}$ surfaces in (b) and (d), respectively. LEEM ROI = 20 μm × 20 μm.
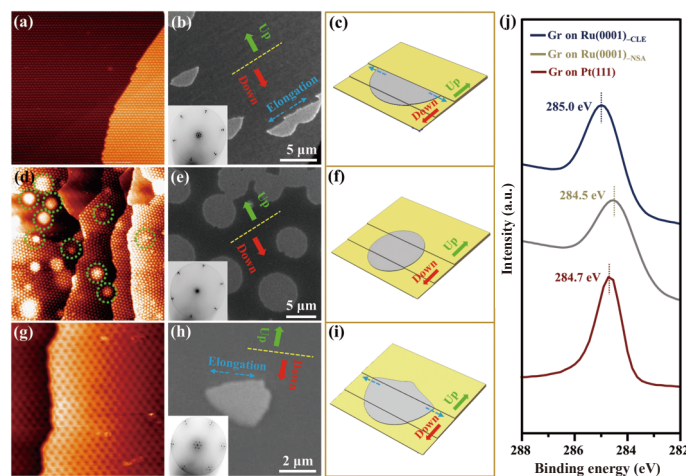
Figure 2 Graphene grown on Ru(0001)$_{-CLE}$, Ru(0001)$_{-NSA}$, and Pt(111) surfaces. (a), (d), and (g) STM images of graphene grown on Ru(0001)$_{-CLE}$ (200 nm × 200 nm), Ru(0001)$_{-NSA}$ (200 nm × 200 nm), and Pt(111) (40 nm × 40 nm) surfaces, respectively. The green dotted circles represent the zone containing near-surface Ar nanobubbles. (b), (e), and (h) LEEM images with inserted LEED patterns of graphene growth on these three surfaces, respectively. The yellow dotted lines indicate the extended direction of surface steps. (c), (f) and (i) Schematics of graphene extension on these three surfaces. The couples of blue dotted arrows display the elongation of graphene domains along the terrace direction. (j) C 1s XPS spectra acquired from graphene on these three surfaces. It's noted that the C 1s XPS spectra from graphene on Ru(0001)$_{-CLE}$ and Ru(0001)$_{-NSA}$ surfaces have been deconvoluted and the raw data is displayed in Fig. S2 in the ESM.

the presence of near-surface Ar nanobubbles remarkably weakens the coupling strength between the graphene overlayers and Ru(0001) surfaces, that is, the out-of-plane interaction [37, 38]. Furthermore, density function theory simulations (Fig. S3 in the ESM) demonstrate that the adsorption energy of graphene on Ru(0001)$_{-NSA}$ surfaces is lower than that on Ru(0001)$_{-CLE}$ surfaces, which decreases with the increase in the height of near-surface Ar nanobubbles. This tendency indicates that the coupling strength of the graphene/Ru(0001) interface is decreased by introducing near-surface Ar nanobubbles, in agreement with XPS and μ-LEED observations.

As a control experiment, we carried out the growth of graphene on Pt(111) as a reference, which is a typical weak interaction regime [7, 29]. The STM and μ-LEED results (Figs. 2(g) and 2(h)) show moiré patterns that are consistent with the coincidence structure with (10 × 10) graphene unit cells matched to (9 × 9) Pt unit cells. As displayed in Figs. 2(h) and 2(i), the graphene can fully grow across the downhill surface steps, but only partly across the uphill steps, indicating a weak in-plane interaction between the Pt(111) steps and graphene domain boundaries. In contrast, the interaction between graphene domain boundaries and Ru(0001)$_{-NSA}$ surface steps is nearly depleted, thus weaker than that of graphene/Pt(111) regimes. Besides, Ru(0001)$_{-NSA}$ surfaces interact with graphene overlayers even more weakly than Pt(111) in the out-of-plane direction. This can be verified by the XPS results for C 1s binding energy in graphene/Ru(0001)$_{-NSA}$, which is 0.2 eV lower than that of graphene/Pt(111) (Fig. 2(j)) [39, 40]. This observation confirms that quasi-freestanding graphene overlayers are achieved on Ru(0001)$_{-NSA}$ surfaces.

Hence, the in-plane interaction strength decreases with the decrease in out-of-plane interaction of graphene/Ru(0001)$_{-CLE}$, graphene/Pt(111), and graphene/Ru(0001)$_{-NSA}$ regimes. Following the observed shape evolution of graphene, it can be deduced that near-surface Ar nanobubbles first weaken the out-of-plane interaction between graphene overlayers and Ru(0001) surfaces,

which facilitates the simultaneous removal of surface-step-dependent in-plane interactions. These two factors contribute to the isotropic growth of graphene with a quasi-freestanding feature, like the growth behavior on liquid substrates [17–20].

To trace the growth process, the sector-shaped graphene growth on Ru(0001)$_{-CLE}$ (Figs. 3(a)–3(c) and Video ESM1) and the round-shaped graphene growth on Ru(0001)$_{-NSA}$ (Figs. 3(d)–3(f) and Video ESM2) were recorded using real-time LEEM images. The growth rate can be evaluated by the equation $v = dA/(L \cdot dt)$, where v is the growth rate, A is the domain area, L is the domain perimeter, and t is the growth time [41, 42]. The quantitative calculation from the statistical data in Figs. 3(g) and 3(h) illustrates that the growth rates of the sector- and round-shaped domains are 3.3 and 6.9 nm/s at 800 °C, respectively. A similar quantitative analysis was conducted for the growth at 850 °C (Fig. S4 in the ESM), which reveals that growth rates of the sector- and round-shaped domains are 4.5 and 10.0 nm/s, respectively. The round-shaped domains extend approximately 2.1–2.2 times faster than the sector-shaped domains because the very weak out-of-plane interaction integrates the growth species into the as-formed graphene domains more easily and the nearly depleted in-plane interaction removes the surface-dependent anisotropy. Hence, the growth of graphene on the Ru(0001)$_{-NSA}$ surface is more kinetically favorable than that on the Ru(0001)$_{-CLE}$ surface. Except the method in our regimes, alloying metal substrates and reducing nucleation amount have proved to be both effective to increase the growth rate [43, 44].

3.2 Coalescence of graphene domains under quasi-freestanding conditions

The round-shaped graphene domains present an isotropic growth behavior, which is expected to serve as an essential intermediate to realize seamless coalescence and further preparation of large-scale graphene single crystals. The coalescing behavior of round-shaped graphene on the Ru(0001)$_{-NSA}$ surface was monitored by real-time
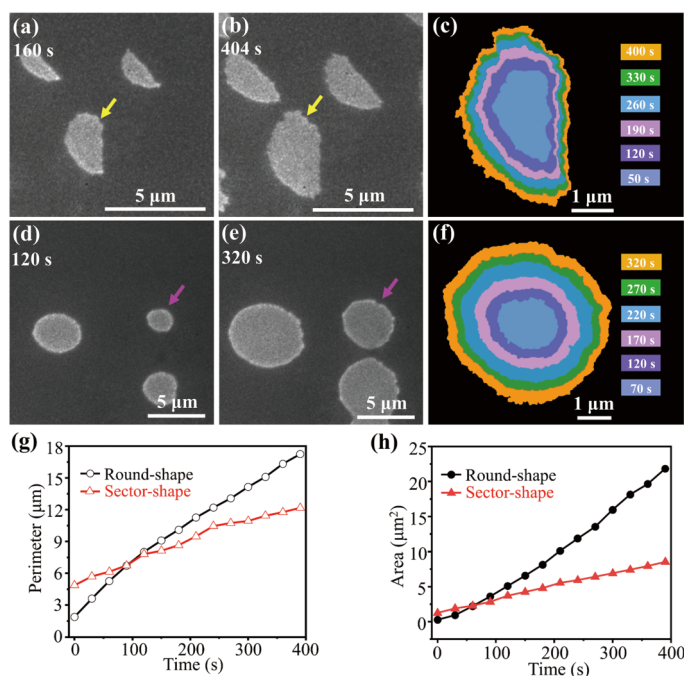
Figure 3 Effect of near-surface Ar nanobubbles on the growth dynamics of graphene. (a) and (b) Snapshots of a LEEM video acquired during graphene growth on the Ru(0001)$_{-CLE}$ surface by exposing to 1.0 × 10^{-8} mbar C$_2$H$_4$ gases at 800 °C for 160 and 404 s, respectively. (d) and (e) Snapshots of a LEEM video acquired during graphene growth on the Ru(0001)$_{-NSA}$ surface under the same conditions for 120 and 320 s, respectively. (c) and (f) Extended growth processes of a sector- and a round-shaped graphene domains, which are marked by a yellow arrow in (a) and a purple arrow in (d), respectively. Evolution of perimeter (g) and area (h) of the sector- and round-shaped graphene domains at 800 °C, labelled by a yellow arrow in (a) and a purple arrow in (d), respectively. The triangles and circles indicate the sector- and round-shaped graphene domains, respectively.

LEEM measurements, and the results are shown in Figs. 4(a)–4(f) and 4(j), and Video ESM3. When two neighboring round-shaped graphene domains approach each other, tips appear at the approaching frontiers, whose morphology changes from a round-shape to a pear-like-shape (Figs. 4(b)–4(d)). The graphene expansion at the approaching frontiers (labelled as d_1 and d_2 in Fig. 4(d)) and in the radial direction (d_3 and d_4 in Fig. 4(d)) are both measured. As shown in Fig. 4(k), both curves d_1 and d_2 are linear within the growth time of 12 s and display quadratic function-like features when the growth time exceeds 12 s, which is ascribed to the growth with a constant rate (labelled by a gray block) and an accelerated growth (labelled by a bluish green block)
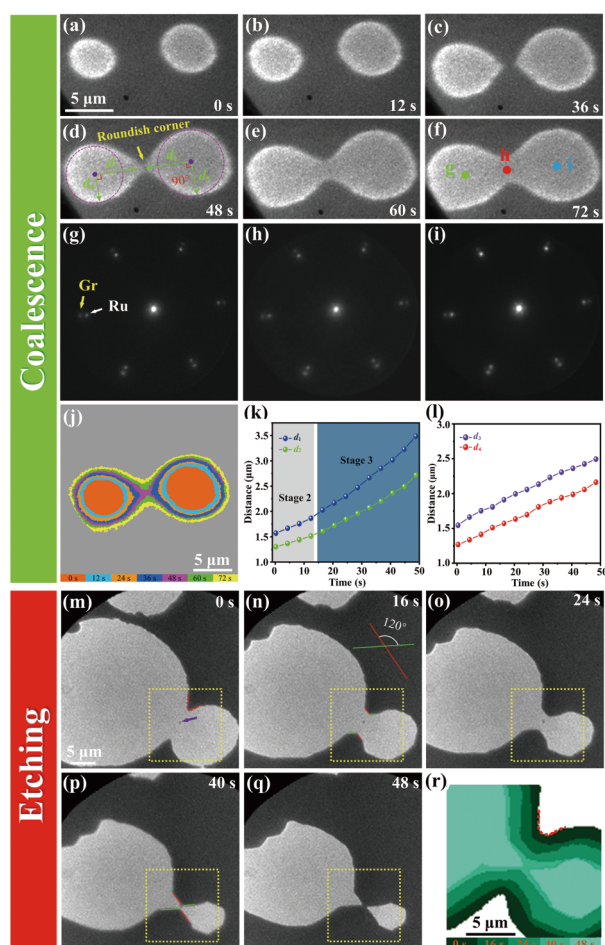

Figure 4 Seamless coalescence of round-shaped graphene domains triggered by near-surface Ar nanobubbles. (a)–(f) Snapshots of a LEEM video recorded during the coalescence of neighboring round-shaped graphene domains on the Ru(0001)$_{-NSA}$ surface by exposure to 1.0×10^{-8} mbar C_2H_4 gases at 850 °C for 0, 12, 36, 48, 60, and 72 s, respectively. (g)–(i) Micron-region LEED patterns of the two round-shaped graphene domains and the stitched zone, marked by three different colored spots in (f). (j) Extended coalescing processes of the neighboring round-shaped graphene domains. (k) Distance from the graphene center to the edge at approaching frontiers as a function of growth time as measured by *in situ* LEEM video, in accordance with the labled d_1 and d_2 in (d). (l) Distance from the graphene center to the edge at the radial direction as a function of growth time measured by *in situ* LEEM video, in accordance with the labled d_3 and d_4 in (d). The radial direction is perpendicular to approaching frontiers. (m)–(q) Snapshots of a LEEM video recorded during the etching of the as-stitched round-shaped graphene domains on the Ru(0001)$_{-NSA}$ surface by exposure to 1.0×10^{-7} mbar O_2 gases at 700 °C for 0, 16, 24, 40, and 48 s, respectively. The spot labelled by a purple arrow in (m) is the defect pixel on screen. (r) Etching evolution of the coalesced graphene domains zooms in the yellow windows in (m)–(q). The red dotted lines in (m) and (r) represent the roundish concave corner at the stitching zone, at the beginning of the etching process.

at the approaching frontiers, respectively. Curves d_3 and d_4 are typically linear functions, and the growth rate remains constant in the radial direction (Fig. 4(l)). It is necessary to point out that no influence of the electron beam during the overlayer growth could be detected. The observed areas and their respective surroundings displayed similar coalescence behavior, as evidenced by moving the sample under the beam or by changing the magnification (Video ESM3).

Owing to the high catalytic activity of Ru(0001)$_{-NSA}$ surfaces, a large number of growth species via C_2H_4 dissociation are generated on the surfaces. The consumption of growth species is less than the supplementation, which leads to an attachment-limited growth process [30, 45]. In addition to the significantly weakened out-of-plane coupling strength and the diminished in-plane surface-step-dependent interaction, the as-formed growth species quickly diffuse and adopt a long immigration lifetime on the surface, finally enriching near the growth front of domains, that is, the enrichment zone. The coalescing behavior is expected to consist of three stages, as shown in Scheme 1. On the heels of graphene nucleation, growth species gather in the area near the growth front and form the enrichment zones. With domain expansion, the length of enrichment zones develops to the maximum until the growth reaches a quasi-equilibrium state (stage 1). This stage proceeds very quickly from nanometer to mesoscale, which is hardly observed. The length of the enrichment zone depends on the immigration lifetime of growth species and their associated diffusion distance on the substrate surface [46]. In stage 2, enrichment zones approach each other before they overlap, and the neighboring domains isotropically expand at a constant rate, which exhibits good agreement with the statistical results labelled by a gray block in Fig. 4(k). Accompanying further expansion of graphene domains, enrichment zones overlap (stage 3) such that the concentration of growth species increases. As a result, the graphene growth is accelerated at the approaching frontiers in accordance with the evolution tendency labelled by a bluish green block in Fig. 4(k), leading to the formation of pear-like domains (stage 3).

In fact, the accelerated growth in the approaching direction is barely observed in the coalescence of 2D materials. Normally, on surfaces with a high hydrocarbon-dissociation activity, such as the Ru(0001)$_{-CLE}$ (strong coupling strength) and the Pt(111) (relatively weak coupling strength), the graphene coalescence follows attachment-limited way, and thus the expansion rate of domains in the approaching direction is constant [15, 30, 45, 47, 48]. In contrast to Ru(0001)$_{-NSA}$ surfaces, the coupling strength of
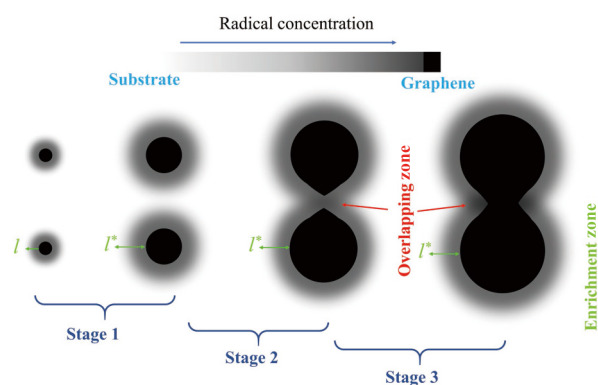
Scheme 1 Schematic of the coalescing mechanism of round-shaped graphene domains. Stage 1: The enrichment zones build up and enlarge to their full size according to the immigration lifetime and diffusion length of building blocks. Stage 2: The enrichment zones approach each other before they overlap, leading to a growth process with a constant rate. Stage 3: The enrichment zones overlap, resulting in an accelerated growth in the approaching front.

Ru(0001)$_{-CLE}$ and Pt(111) surfaces is not sufficiently weak to achieve a long immigration lifetime of growth species. Therefore, the enrichment zone cannot be developed and no growth acceleration is observed [9, 15, 38, 49]. On the other hand, surfaces with a low hydrocarbon-dissociation activity, such as the Cu surface adopting a weak out-of-plane coupling strength, result in a shortage of growth species near graphene domain boundaries from a surface-diffusion-limited process [7, 50, 51]. The immigration lifetime of growth species is very short on the Cu surface [46]. Thus, capture zones without abundant growth species are generated near graphene domain boundaries. When two graphene domains approach each other, the two capture zones overlap, causing an increase in the consumption of growth species and further a decelerated growth behavior at the approaching frontiers [46].

During coalescence, the roundish concave corner appears at the stitching zone, as shown in Fig. 4(d). Wang et al. have confirmed that the appearance of the roundish concave corner in the stitching zone can be regarded as an indicator of the seamless coalescence of 2D overlayers on weakly interacting surfaces [39, 52]. After coalescence, μ-LEED was applied to detect the two graphene domains and the stitched area. The results show that the three zones have the same orientation, that is, graphene aligned with the Ru(0001) surfaces adopted a weak $(13 \times 13)_{-graphene}$ on $(12 \times 12)_{-Ru}$ moiré superstructure (Figs. 4(g)–4(i)). Accordingly, it can be deduced that the coalescence of graphene on Ru(0001)$_{-NSA}$ surfaces follows a seamless route, due to the very weak overlayer–substrate interaction, the appearance of the roundish concave corner in the stitching zone, and the same orientation. In contrast, seamless coalescence of graphene is hardly achieved on strong interacting regimes such as Rh(111) and Co(0001) surfaces, which needs both an identical orientation of the graphene lattice and the coherence of the moiré corrugation of the respective domains because alternating adsorption sites induce a substantial periodic buckling in the form of a large moiré corrugation [39, 53]. From this perspective, on Ru(0001)$_{-CLE}$ surfaces similar to Rh(111) surfaces, seamlessly coalescing behaviors are expected to be unavailable, although the graphene domains expand in an identical orientation [38]. Thus, the "imperfect to seamless" coalescence transition is realized through significantly weakening overlayer–substrate interaction induced by near-surface Ar nanobubbles on Ru(0001) surfaces.

To further elucidate the seamless coalescence, the as-stitched graphene domains are etched by O$_2$ atmospheres, in which the atmosphere exhibits a high etching efficiency under UHV conditions (Figs. 4(m)–4(q) and Video ESM4) [54]. It has been observed that the roundish concave corner forms at the stitching zone, at the beginning of the etching process (Figs. 4(m) and 4(r)). The concave corners present an angle of 120° at the stitching zone (Figs. 4(n) and 4(p)) during etching, which indicates that the two domains are aligned. Moreover, the formation of the vacancy domains or cracking was not observed at the stitching zone during the entire etching process, which implies that there is no grain boundary in the stitching area. This etching behavior further confirms that the observed coalescence of 2D overlayers is seamless [39, 55, 56]. Hence, the seamless coalescence of graphene domains on Ru(0001)$_{-NSA}$ surfaces can be reassured.

3.3 Etching-regrowth behavior of graphene overlayers under quasi-freestanding conditions

The formation of quasi-freestanding graphene offers a practical way to investigate the intrinsic evolution behavior. Generally, etching of 2D overlayers is an efficient manner for analyzing their evolution mechanism. In particular, etching in the quasi-thermodynamic equilibrium condition assists in attaining the

Wulff structure of 2D overlayers [49, 57–59]. Under real reaction conditions, the evolution behavior of graphene is disturbed by non-ideal factors such as defects and surface step restriction, resulting in distortions on the domain morphology that leads to a structure different from the Wulff structure [35, 36]. For example, sector-shaped graphene domains on Ru(0001)$_{-CLE}$ retain their own shape when etched using O$_2$ gas at different temperatures and pressures, which is caused by the strong surface step restriction, as shown by the etching process under typical conditions in Fig. S5 in the ESM. In contrast, when etching round-shaped graphene domains on Ru(0001)$_{-NSA}$ under the same conditions, the graphene morphology changes from a round shape to a hexagon shape (Figs. 5(a)–5(f) and Video ESM5), implying the formation of a graphene Wulff construction [60, 61].

Studies have reported that the edges of round-shaped domains consist of three different structures, including zigzag, armchair, and S19° (with a rotation angle of ~ 19° with respect to the zigzag edge) edges [62–64]. The stabilization energies of these three edges increase successively because of the increase in kink density [62–64]. Because the interfacial interaction between graphene and the Ru(0001) surface is significantly weakened by near-surface Ar nanobubbles, graphene overlayers are quasi-freestanding and display intrinsic properties [20, 65]. Ru(0001) surfaces adopt a high catalytic activity for the decomposition of O$_2$ into O atoms, which provides sufficient etching agents [54]. These two effects contribute to attaining the quasi-thermodynamic equilibrium state. Hence, following the above-mentioned difference of these three edge structures in energy stabilization, the etching rates of the zigzag, armchair, and S19° edges orderly increase, resulting in that the proportion of zigzag edges in these three edge structures successively increases and finally only the zigzag edges are preserved (Fig. 5(c) and Schemes 2(a) and 2(c)). Correspondingly,
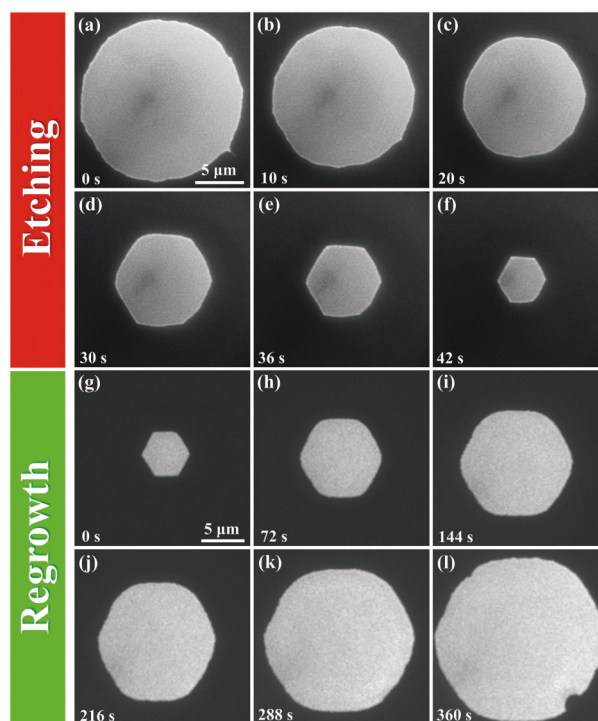
Figure 5 Morphology and edge evolution of graphene domains on the Ru(0001)$_{-NSA}$ surface during O$_2$ etching and regrowth by introducing C$_2$H$_4$ gases. (a)–(f) Snapshots of a LEEM video acquired from a round-shaped graphene domain etching by 1.0×10^{-7} mbar O$_2$ gases at 700 °C on the Ru(0001)$_{-NSA}$ surface for 0, 10, 20, 30, 36, and 42 s, respectively. (g)–(i) Snapshots of a LEEM video acquired during a hexagon-shaped graphene domain regrowing by introducing 5.0×10^{-9} mbar C$_2$H$_4$ gases at 700 °C on the Ru(0001)$_{-NSA}$ surface for 0, 72, 144, 216, 288, and 360 s, respectively.

the graphene morphology changes from a round shape to a truncated hexagon (dodecagon) shape and eventually the hexagon shape, that is, the Wulff construction (Fig. 5(f) and Schemes 2(a) and 2(c)) [62]. This etching process reveals the intrinsic evolution behavior of graphene in the freestanding condition. Hence, the etching competition among the three different edges of the round-shaped graphene overlayer determines the final graphene morphology.

In addition, the regrowth originating from the hexagonal graphene domain was performed by introducing 5.0×10^{-9} mbar C_2H_4 gases at 700 °C. It is a reversible process with respect to the above-mentioned etching; thus, the graphene shape changes from hexagon to trunted hexagon (dodecagon), and eventually quasi-round, that is, icosikaitetragon (Figs. 5(g)–5(l) and Video ESM6). The edge structures of graphene transform from the zigzag-terminated edge to the zigzag, armchair, and S19° mixture-terminated edge (Schemes 2(b) and 2(c)). Owing to the quasi-freestanding condition, attachment barriers during the integration of growth species into these three types of edges are nearly equivalent. Thus, the growth kinetics of these edges are almost identical, which induces a growth mode transformation from anisotropic to isotropic way, that is, a "hexagon to round" morphological transition.

It is worth mentioning that previous *ex situ* studies have captured segmental images of this shape transition under ambient to near-ambient pressure [51, 62]. In our regime the "round to hexagon" morphological transition by etching-regrowth has been observed in real-time under UHV conditions. Our study draws a complete picture of this evolution behavior, which provides detailed clues to the systematic understanding of the morphological transition in freestanding conditions. Moreover, the realization of this evolution behavior from UHV to ambient conditions indicates that the pressure gap can be fully bridged, which is in good agreement with our previous studies [39, 59].

4 Conclusions
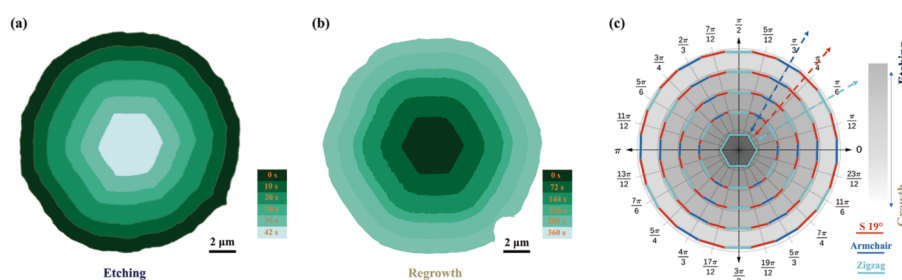
Scheme 2 Schematic of the graphene morphology transition processes for etching (a) and regrowth (b), according to Fig. 5. (c) Edge evolution of graphene domains on the Ru(0001)$_{-NSA}$ surface during the etching and regrowth. The colored dotted arrows represent the evolution directions of the zigzag, armchair, and S19° edges, respectively.

Overall, the appearance of the round-shaped graphene domain is a sign of the isotropic growth mode, which is a mesoscopic expression of the nearly depleted overlayer–substrate interaction, i.e., the quasi-freestanding condition. Under this condition, all of the typical edges including zigzag, armchair, and S19° edge structures are energetically favorable in their respective directions. Considering graphene as a prototype of 2D films, we deduce that the results which we observed here can be generalized to all other 2D crystalline materials. Indeed, round-shaped domains also appear during the formation of h-BN and transition metal dichalcogenides (TMDs). Previous reports have confirmed that graphene can grow in an isotropic mode on liquid substrates, such as molten metal or molten insulators (glass) [17–20]. Lee et al. have achieved the preparation of round-shaped h-BN on liquid Au substrate [18]. The MoS_2 domains with a round shape also have also been observed on SiO_2/Si substrates [66].

The round-shaped graphene domain plays as an essential intermediate for seamless coalescence and further preparation of large-scale graphene single crystals. For example, Zeng et al. and Lee et al. achieved these goals for graphene on liquid Cu substrates and h-BN on liquid Au substrates, respectively [17, 18]. In our case, near-surface Ar nanobubbles remarkably weaken interfacial interactions between graphene and Ru(0001) such that the solid Ru(0001) surfaces serve the similar roles as the liquid substrates, resulting in isotropic growth and seamless coalescence of graphene as well as the "round to hexagon" morphological transition by etching-regrowth. In addition, Ru(0001)$_{-NSA}$ surfaces possess the following advantages in comparison with normal liquid substrates including Cu, Au, and glass. First, it's more energy-efficient and economically viable because Ru(0001)$_{-NSA}$ surfaces have higher catalytic activity for the decomposition of precursor gases and etching gases, contributing to lower growth (or etching) temperatures and lower growth pressures [17, 18, 20, 41]. Second, our method is more simply operated owing to the solid surface. In addition, we also observed the isotropic growth of h-BN on Ru(0001)$_{-NSA}$ surfaces (Fig. S6 in the ESM), and similar coalescence, etching, and regrowth processes can be expected [67]. Accordingly, isotropic growth, seamless coalescence, and Wulff construction should be realized in other 2D overlayers such as TMDs and carbides on Ru(0001) surfaces containing near-surface Ar nanobubbles under free-standing conditions. The *in situ* surface imaging at multiple scales, surface spectroscopy, depth-resolution mass spectrum experiments, and DFT calculations presented here reveal the interfacial-interaction-dependent dynamic nature of the process in an unparalleled way and provide important insights into the insintric kinetic evolution behavior from the micro- to nanometer scale.

10.1007/s12274-021-3731-2.

References

[1] Schwierz, F. Industry-compatible graphene transistors. *Nature* **2011**, *472*, 41–42.

[2] Chen, J. H.; Ishigami, M.; Jang, C.; Hines, D. R.; Fuhrer, M. S.; Williams, E. D. Printed graphene circuits. *Adv. Mater.* **2007**, *19*, 3623–3627.

[3] Bonaccorso, F.; Sun, Z.; Hasan, T.; Ferrari, A. C. Graphene photonics and optoelectronics. *Nat. Photonics* **2010**, *4*, 611–622.

[4] Li, X. S.; Cai, W. W.; An, J. B.; Kim, S.; Nah, J.; Yang, D. X.; Piner, R.; Velamakanni, A.; Jung, I.; Tutuc, E. et al. Large-area synthesis of high-quality and uniform graphene films on copper foils. *Science* **2009**, *324*, 1312–1314.

[5] Reina, A.; Jia, X. T.; Ho, J.; Nezich, D.; Son, H.; Bulovic, V.; Dresselhaus, M. S.; Kong, J. Large area, few-layer graphene films on arbitrary substrates by chemical vapor deposition. *Nano Lett.* **2009**, *9*, 30–35.

[6] Wintterlin, J.; Bocquet, M. L. Graphene on metal surfaces. *Surf. Sci.* **2009**, *603*, 1841–1852.

[7] Batzill, M. The surface science of graphene: Metal interfaces, CVD synthesis, nanoribbons, chemical modifications, and defects. *Surf. Sci. Rep.* **2012**, *67*, 83–115.

[8] Qin, B.; Ma, H. F.; Hossain, M.; Zhong, M. Z.; Xia, Q. L.; Li, B.; Duan, X. D. Substrates in the synthesis of two-dimensional materials via chemical vapor deposition. *Chem. Mater.* **2020**, *32*, 10321–10347.

[9] Sutter, P.; Sutter, E. Microscopy of graphene growth, processing, and properties. *Adv. Funct. Mater.* **2013**, *23*, 2617–2634.

[10] Sutter, P. W.; Flege, J. I.; Sutter, E. A. Epitaxial graphene on ruthenium. *Nat. Mater.* **2008**, *7*, 406–411.

[11] Miniussi, E.; Pozzo, M.; Mentes, T. O.; Niño, M. A.; Locatelli, A.; Vesselli, E.; Comelli, G.; Lizzit, S.; Alfè, D.; Baraldi, A. The competition for graphene formation on Re(0001): A complex interplay between carbon segregation, dissolution and carburisation. *Carbon* **2014**, *73*, 389–402.

[12] Günther, S.; Dänhardt, S.; Wang, B.; Bocquet, M. L.; Schmitt, S.; Wintterlin, J. Single terrace growth of graphene on a metal surface. *Nano Lett.* **2011**, *11*, 1895–1900.

[13] Meng, C. X.; Gao, J. F.; Li, R. T.; Ning, Y. X.; Chang, Y.; Mu, R. T.; Fu, Q.; Bao, X. H. Step-confined thin film growth via near-surface atom migration. *Nano Res.* **2020**, *13*, 1552–1557.

[14] Yu, Q. K.; Jauregui, L. A.; Wu, W.; Colby, R.; Tian, J. F.; Su, Z. H.; Cao, H. L.; Liu, Z. H.; Pandey, D.; Wei, D. G. et al. Control and characterization of individual grains and grain boundaries in graphene grown by chemical vapour deposition. *Nat. Mater.* **2011**, *10*, 443–449.

[15] Sutter, P.; Sadowski, J. T.; Sutter, E. Graphene on Pt(111): Growth and substrate interaction. *Phys. Rev. B* **2009**, *80*, 245411.

[16] Coraux, J.; N'Diaye, A. T.; Engler, M.; Busse, C.; Wall, D.; Buckanie, N.; zu Heringdorf, F. J. M.; van Gastel, R.; Poelsema, B.; Michely, T. Growth of graphene on Ir(111). *New J. Phys.* **2009**, *11*,

023006.

[17] Zeng, M. Q.; Tan, L. F.; Wang, L. X.; Mendes, R. G.; Qin, Z. H.; Huang, Y. X.; Zhang, T.; Fang, L. W.; Zhang, Y. F.; Yue, S. L. et al. Isotropic growth of graphene toward smoothing stitching. *ACS Nano* **2016**, *10*, 7189–7196.

[18] Lee, J. S.; Choi, S. H.; Yun, S. J.; Kim, Y. I.; Boandoh, S.; Park, J. H.; Shin, B. G.; Ko, H.; Lee, S. H.; Kim, Y. M. et al. Wafer-scale single-crystal hexagonal boron nitride film via self-collimated grain formation. *Science* **2018**, *362*, 817–821.

[19] Liu, B. Z.; Wang, H. H.; Gu, W.; Zhou, L.; Chen, Z. L.; Nie, Y. F.; Tan, C. W.; Ci, H. N.; Wei, N.; Cui, L. Z. et al. Oxygen-assisted direct growth of large-domain and high-quality graphene on glass targeting advanced optical filter applications. *Nano Res.* **2021**, *14*, 260–267.

[20] Chen, Y. B.; Sun, J. Y.; Gao, J. F.; Du, F.; Han, Q.; Nie, Y. F.; Chen, Z. L.; Bachmatiuk, A.; Priydarshi, M. K.; Ma, D. L. et al. Growing uniform graphene disks and films on molten glass for heating devices and cell culture. *Adv. Mater.* **2015**, *27*, 7839–7846.

[21] Weatherup, R. S.; Amara, H.; Blume, R.; Dlubak, B.; Bayer, B. C.; Diarra, M.; Bahri, M.; Cabrero-Vilatela, A.; Caneva, S.; Kidambi, P. R. et al. Interdependency of subsurface carbon distribution and graphene-catalyst interaction. *J. Am. Chem. Soc.* **2014**, *136*, 13698–13708.

[22] Wei, W.; Lin, L.; Zhang, G. H.; Ye, X. Q.; Bin, R.; Meng, C. X.; Ning, Y. X.; Fu, Q.; Bao, X. H. Effect of near-surface dopants on the epitaxial growth of h-BN on metal surfaces. *Adv. Mater. Interfaces* **2019**, *6*, 1801906.

[23] Kohn, W.; Becke, A. D.; Parr, R. G. Density functional theory of electronic structure. *J. Phys. Chem.* **1996**, *100*, 12974–12980.

[24] Kresse, G.; Furthmüller, J. Efficient iterative schemes for *ab initio* total-energy calculations using a plane-wave basis set. *Phys. Rev. B* **1996**, *54*, 11169–11186.

[25] Blöchl, P. E. Projector augmented-wave method. *Phys. Rev. B* **1994**, *50*, 17953–17979.

[26] Kresse, G.; Joubert, D. From ultrasoft pseudopotentials to the projector augmented-wave method. *Phys. Rev. B* **1999**, *59*, 1758–1775.

[27] Perdew, J. P.; Burke, K.; Ernzerhof, M. Generalized gradient approximation made simple. *Phys. Rev. Lett.* **1996**, *77*, 3865–3868.

[28] Grimme, S.; Ehrlich, S.; Goerigk, L. Effect of the damping function in dispersion corrected density functional theory. *J. Comput. Chem.* **2011**, *32*, 1456–1465.

[29] Preobrajenski, A. B.; Ng, M. L.; Vinogradov, A. S.; Mårtensson, N. Controlling graphene corrugation on lattice-mismatched substrates. *Phys. Rev. B* **2008**, *78*, 073401.

[30] Kirsch, H.; Tong, Y. J.; Campen, R. K. Experimental characterization of CCH(ads) and CCH₂(ads) during the thermal decomposition of methane and ethylene on Ru(0001). *Chem Cat Chem* **2016**, *8*, 728–735.

[31] Ren, Y.; Waluyo, I.; Beale, E.; Trenary, M. Hydrogenation and dehydrogenation reactions of C_2H_x moieties on the Ru(001) surface. *Surf. Sci.* **2016**, *650*, 144–148.

[32] Gsell, M.; Jakob, P.; Menzel, D. Effect of substrate strain on adsorption. *Science* **1998**, *280*, 717–720.

[33] Locatelli, A.; Menteş, T. O. Chemical and magnetic imaging with X-ray photoemission electron microscopy. In *Synchrotron Radiation*; Mobilio, S.; Boscherini, F.; Meneghini, C., Eds.; Springer: Berlin, Heidelberg, 2015; pp 571−591.

[34] Tchaplyguine, M.; Feifel, R.; Marinho, R. R. T.; Gisselbrecht, M.; Sorensen, S. L.; de Brito, A. N.; Mårtensson, N.; Svensson, S.; Björneholm, O. Selective probing of the electronic structure of free clusters using resonant core-level spectroscopy. *Chem. Phys.* **2003**, *289*, 3–13.

[35] Sutter, P.; Hybertsen, M. S.; Sadowski, J. T.; Sutter, E. Electronic structure of few-layer epitaxial graphene on Ru(0001). *Nano Lett.* **2009**, *9*, 2654–2660.

[36] McCarty, K. F.; Feibelman, P. J.; Loginova, E.; Bartelt, N. C. Kinetics and thermodynamics of carbon segregation and graphene growth on Ru(0 0 0 1). *Carbon* **2009**, *47*, 1806–1813.

[37] Zhang, Y. H.; Weng, X. F.; Li, H.; Li, H. B.; Wei, M. M.; Xiao, J. P.; Liu, Z.; Chen, M. S.; Fu, Q.; Bao, X. H. Hexagonal boron nitride cover on Pt(111): A new route to tune molecule-metal interaction

and metal-catalyzed reactions. *Nano Lett.* **2015**, *15*, 3616–3623.

[38] Yang, Y.; Fu, Q.; Wei, M. M.; Bluhm, H.; Bao, X. H. Stability of BN/metal interfaces in gaseous atmosphere. *Nano Res.* **2015**, *8*, 227–237.

[39] Wang, Z. J.; Dong, J. C.; Li, L. F.; Dong, G. C.; Cui, Y.; Yang, Y.; Wei, W.; Blume, R.; Li, Q.; Wang, L. et al. The coalescence behavior of two-dimensional materials revealed by multiscale *in situ* imaging during chemical vapor deposition growth. *ACS Nano* **2020**, *14*, 1902–1918.

[40] Addou, R.; Dahal, A.; Batzill, M. Growth of a two-dimensional dielectric monolayer on quasi-freestanding graphene. *Nat. Nanotechnol.* **2013**, *8*, 41–45.

[41] Starodub, E.; Bartelt, N. C.; McCarty, K. F. Oxidation of graphene on metals. *J. Phys. Chem. C* **2010**, *114*, 5134–5140.

[42] Wei, W.; Meng, C. X.; Fu, Q.; Bao, X. H. Intercalation-etching of graphene on Pt(111) in H_2 and O_2 observed by *in-situ* low energy electron microscopy. *Sci. China Chem.* **2017**, *60*, 656–662.

[43] Lu, G. Y.; Wu, T. R.; Yuan, Q. H.; Wang, H. S.; Wang, H. M.; Ding, F.; Xie, X. M.; Jiang, M. H. Synthesis of large single-crystal hexagonal boron nitride grains on Cu-Ni alloy. *Nat. Commun.* **2015**, *6*, 6160.

[44] Xu, X. Z.; Zhang, Z. H.; Qiu, L.; Zhuang, J. N.; Zhang, L.; Wang, H.; Liao, C. N.; Song, H. D.; Qiao, R. X.; Gao, P. et al. Ultrafast growth of single-crystal graphene assisted by a continuous oxygen supply. *Nat. Nanotechnol.* **2016**, *11*, 930–935.

[45] Loginova, E.; Bartelt, N. C.; Feibelman, P. J.; McCarty, K. F. Evidence for graphene growth by C cluster attachment. *New J. Phys.* **2008**, *10*, 093026.

[46] Wang, Z. J.; Weinberg, G.; Zhang, Q.; Lunkenbein, T.; Klein-Hoffmann, A.; Kurnatowska, M.; Plodinec, M.; Li, Q.; Chi, L. F.; Schloegl, R. et al. Direct observation of graphene growth and associated copper substrate dynamics by *in situ* scanning electron microscopy. *ACS Nano* **2015**, *9*, 1506–1519.

[47] Navin, J. K.; Donald, S. B.; Tinney, D. G.; Cushing, G. W.; Harrison, I. Communication: Angle-resolved thermal dissociative sticking of CH_4 on Pt(111): Further indication that rotation is a spectator to the gas-surface reaction dynamics. *J. Chem. Phys.* **2012**, *136*, 061101.

[48] Harris, J.; Luntz, A. C. Tunneling-mediated dissociation at metal surfaces. *Mod. Phys. Lett. B* **1991**, *5*, 1953–1962.

[49] Wang, Z. J.; Ding, F.; Eres, G.; Antonietti, M.; Schloegl, R.; Willinger, M. G. Formation mechanism, growth kinetics, and stability limits of graphene adlayers in metal-catalyzed CVD growth. *Adv. Mater. Interfaces* **2018**, *5*, 1800255.

[50] Sun, Y. Y. L.; Zhang, S.; Zhang, W. H.; Li, Z. Y. Theoretical study of adsorption and dehydrogenation of C_2H_4 on Cu(410). *Chin. J. Chem. Phys.* **2018**, *31*, 485–491.

[51] Wu, B.; Geng, D. C.; Xu, Z. P.; Guo, Y. L.; Huang, L. P.; Xue, Y. Z.; Chen, J. Y.; Yu, G.; Liu, Y. Q. Self-organized graphene crystal patterns. *NPG Asia Mater.* **2013**, *5*, e36.

[52] Dong, G. C.; Frenken, J. W. M. Kinetics of graphene formation on Rh(111) investigated by *in situ* scanning tunneling microscopy. *ACS Nano* **2013**, *7*, 7028–7033.

[53] Xu, Z. G.; Tian, H.; Khanaki, A.; Zheng, R. J.; Suja, M.; Liu, J. L. Large-area growth of multi-layer hexagonal boron nitride on polished cobalt foils by plasma-assisted molecular beam epitaxy. *Sci. Rep.* **2017**, *7*, 43100.

[54] Blume, R.; Niehus, H.; Conrad, H.; Böttcher, A.; Aballe, L.; Gregoratti, L.; Barinov, A.; Kiskinova, M. Identification of subsurface oxygen species created during oxidation of Ru(0001). *J. Phys. Chem. B* **2005**, *109*, 14052–14058.

[55] Sekerka, R. F. Equilibrium and growth shapes of crystals: How do they differ and why should we care? *Cryst. Res. Technol.* **2005**, *40*, 291–306.

[56] Wang, L.; Xu, X. Z.; Zhang, L. N.; Qiao, R. X.; Wu, M. H.; Wang, Z. C.; Zhang, S.; Liang, J.; Zhang, Z. H.; Zhang, Z. B. et al. Epitaxial growth of a 100-square-centimetre single-crystal hexagonal boron nitride monolayer on copper. *Nature* **2019**, *570*, 91–95.

[57] Zhang, Y.; Li, Z.; Kim, P.; Zhang, L. Y.; Zhou, C. W. Anisotropic hydrogen etching of chemical vapor deposited graphene. *ACS Nano* **2012**, *6*, 126–132.

[58] Dobrik, G.; Tapasztó, L.; Biró, L. P. Selective etching of armchair edges in graphite. *Carbon* **2013**, *56*, 332–338.

[59] Wang, Z. J.; Dong, J. C.; Cui, Y.; Eres, G.; Timpe, O.; Fu, Q.; Ding, F.; Schloegl, R.; Willinger, M. G. Stacking sequence and interlayer coupling in few-layer graphene revealed by *in situ* imaging. *Nat. Commun.* **2016**, *7*, 13256.

[60] Zhang, X. Y.; Li, H.; Ding, F. Self-assembly of carbon atoms on transition metal surfaces-chemical vapor deposition growth mechanism of graphene. *Adv. Mater.* **2014**, *26*, 5488–5495.

[61] Artyukhov, V. I.; Hao, Y. F.; Ruoff, R. S.; Yakobson, B. I. Breaking of symmetry in graphene growth on metal substrates. *Phys. Rev. Lett.* **2015**, *114*, 115502.

[62] Ma, T.; Ren, W. C.; Zhang, X. Y.; Liu, Z. B.; Gao, Y.; Yin, L. C.; Ma, X. L.; Ding, F.; Cheng, H. M. Edge-controlled growth and kinetics of single-crystal graphene domains by chemical vapor deposition. *Proc. Natl. Acad. Sci. USA* **2013**, *110*, 20386–20391.

[63] Artyukhov, V. I.; Liu, Y. Y.; Yakobson, B. I. Equilibrium at the edge and atomistic mechanisms of graphene growth. *Proc. Natl. Acad. Sci. USA* **2012**, *109*, 15136–15140.

[64] Liu, Y. Y.; Dobrinsky, A.; Yakobson, B. I. Graphene edge from armchair to zigzag: The origins of nanotube chirality? *Phys. Rev. Lett.* **2010**, *105*, 235502.

[65] Zeng, M. Q.; Tan, L. F.; Wang, J.; Chen, L. F.; Rümmeli, M. H.; Fu, L. Liquid metal: An innovative solution to uniform graphene films. *Chem. Mater.* **2014**, *26*, 3637–3643.

[66] Xie, S.; Xu, M. S.; Liang, T.; Huang, G. W.; Wang, S. P.; Xue, G. B.; Meng, N.; Xu, Y.; Chen, H. Z.; Ma, X. Y. et al. A high-quality round-shaped monolayer MoS_2 domain and its transformation. *Nanoscale* **2016**, *8*, 219–225.

[67] Wei, W.; Meng, J.; Meng, C. X.; Ning, Y. X.; Li, Q. X.; Fu, Q.; Bao, X. H. Abnormal growth kinetics of h-BN epitaxial monolayer on Ru(0001) enhanced by subsurface Ar species. *Appl. Phys. Lett.* **2018**, *112*, 171601.